Charge lifetime improvement of the Continuous Electron Beam Accelerator Facility photogun with a biased anode

J. T. Yoskowitz[1,2,*] G. A. Krafft[1,3] G. Palacios-Serrano[1,3] S. A. K. Wijethunga[1,3]
J. Grames[3] J. Hansknecht[3,†] C. Hernandez-Garcia[3] M. Poelker[3] M. L. Stutzman[3]
R. Suleiman[3] C. A. Valerio-Lizarraga[4] and S. B. Van Der Geer[5]

[1]*Old Dominion University, Norfolk, Virginia 23529, USA*
[2]*Los Alamos National Laboratory, Los Alamos, New Mexico 87545, USA*
[3]*Thomas Jefferson National Accelerator Facility, Newport News, Virginia 23606, USA*
[4]*Facultad de Ciencias Físico-Matemáticas UAS, 80000 Culiacán, Sinaloa, Mexico*
[5]*Pulsar Physics, Eindhoven, The Netherlands*

GaAs photocathodes in dc high-voltage photoguns are highly susceptible to ion back-bombardment, which reduces the photocathode quantum efficiency and limits the useful operating lifetime for producing polarized electron beams. This paper demonstrates that applying a small positive bias to the photogun anode can significantly suppress ion back-bombardment and increase charge lifetime. This technique was studied extensively using the Continuous Electron Beam Accelerator Facility photogun, where highly polarized electron beams created using a strained-superlattice GaAs/GaAsP photocathode were used and charge lifetimes improved by almost a factor of 2. A new simulation code IONATOR was developed to model ion production and tracking in order to better understand and explain the factors that led to the performance improvement. Results of the experiments and simulations are discussed in detail.

I. INTRODUCTION

GaAs-based dc high-voltage photoguns are critical for the creation of spin-polarized electron beams, which are essential to studying the spin dependence of fundamental interactions, searching for physics beyond the standard model, measuring nucleon structure functions, and studying nuclear matter [1–4]. Consequently, GaAs photocathodes used in photoguns that produce polarized electron beams must perform reliably and, in particular, should exhibit long operating lifetimes. Lifetime is a metric that describes the reduction of photocathode quantum efficiency (QE). For accelerator operations at the Continuous Electron Beam Accelerator Facility (CEBAF) [5], where beam currents can reach 200 μA, operating for 4 weeks means providing 500 C of charge before the QE drops appreciably.

The operating lifetime of modern dc high-voltage GaAs photoguns, operating under ultrahigh vacuum conditions and exhibiting no field emission, is limited by ion back-bombardment (IBB), the process whereby electrically neutral gases

present in the accelerator vacuum beamline are ionized by the electron beam and are subsequently accelerated "back" to the photocathode. During IBB, energetic ions can sputter away activation chemicals on the photocathode surface and/or chemically alter the photocathode material via implantation within the working volume where optical absorption and electron transport occur, each of which can lead to decreased photocathode QE [6–8]. Additionally, energetic ions striking any inner surface of the photogun can liberate residual neutral gases [9], leading to further IBB.

The metric used in this paper to characterize the rate of QE degradation is charge lifetime, which represents the amount of electron beam charge that is extracted before the photocathode QE falls to $1/e$ of its initial value. It is not unusual to use a photocathode for two charge lifetimes, or until the QE drops to about a tenth of its initial value, before intervention is required.

The charge lifetime can be calculated by making repeated measurements of the photocathode QE over the course of beam operations and then fitting the measurements using the formula:

$$\text{QE}(Q) = \text{QE}_0 \exp\left[-\frac{Q}{\tau}\right], \qquad (1)$$

where τ is the charge lifetime of the photocathode, Q is the charge extracted, and QE_0 is the initial QE. The exponential
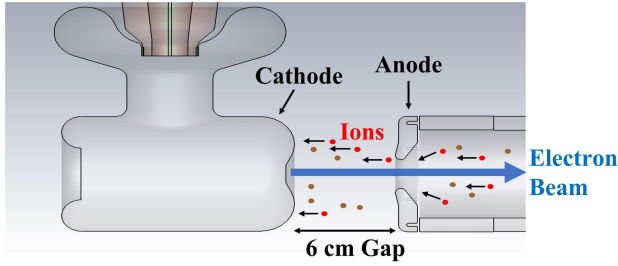
FIG. 1.   Visual model of ions (red) generated by electrons (blue) ionizing residual gas (brown) in a dc high-voltage photogun, distinguishing ions that are created within the cathode-anode gap from those created downstream, which must pass through the anode aperture to result in ion bombardment.

behavior derives from the characteristic that the relative reduction in QE is proportional to the extracted charge. In a dc high-voltage photogun, ions are continuously generated along the electron beam path (see Fig. 1). The ion production rate per unit length (R_{ions}) is proportional to the electron beam current I divided by the electron charge e, the residual gas pressure(s) P_{gas}, and the cross section of electron-impact ionization σ_{impact}, which depends on the gas species and beam energy:

$$R_{ions} = P_{gas} \times \sigma_{impact} \times \frac{I}{e}. \tag{2}$$

Notably, ions formed within the cathode-anode gap are accelerated toward the photocathode, reaching it with a fraction of the cathode potential, whereas ions formed downstream of the anode can reach the photocathode with the full cathode potential if they pass through the anode aperture.

At Jefferson Lab, we have explored various methods to improve charge lifetime by limiting IBB. Improving photogun vacuum has consistently proven to be the most effective approach. However, when vacuum cannot readily be improved further, other means have been used to enhance charge lifetime: (a) positioning the drive laser (and electron emission) away from the electrostatic center (EC) of the cathode-anode lens where ions are focused, (b) limiting the photocathode active area to suppress photoemission from regions of the photocathode that do not support efficient beam delivery and may result in beam loss, and (c) increasing the laser beam size to distribute ions over a larger area where the electron emission occurs [10].

Importantly, ions generated in the vacuum beamline downstream of the photogun are an important concern in accelerators where trapped ions may lead to harmful effects. This is especially true in storage rings where the beam potential readily traps ionized gas. There, the use of a biased electrostatic precipitator to extract ions from the vacuum space is widely used. For example, the Cornell group studied a variety of methods to force ions trapped by

the beam potential away from the photogun in a high current photoinjector [11], including adding a clearing electrode to force ions created downstream of the photogun away from the beam potential. Notably, the precipitator eliminated high-voltage arcing due to ions reaching the photogun cathode-anode gap. In addition, offsetting the anode to repel high energy ions from reaching the photocathode has been proposed [12].

Furthermore, a number of groups have continued exploring altered GaAs surface activation chemistry to enhance QE lifetime [13–17] or photocathode cooling to mitigate laser heating effects for high average power operation [18].

Alternatively, ions can be repelled from reaching the cathode-anode gap by applying a positive bias potential to the anode of the photogun. This method was explored at Brookhaven [19] and at Jefferson Lab [20,21], where the charge lifetime of a bulk GaAs photocathode operating with 532 nm and producing 2–5 mA dc current was studied when the photogun anode was biased or grounded. In this exploratory study, the charge lifetime improved by ∼22% at the EC. However, no improvement was observed when the beam emission location was displaced from the EC. This approach was not pursued further because at CEBAF, the beam emission is purposely displaced from the EC to avoid the relatively poor lifetime there due to IBB. Later, in 2022, the BNL group also confirmed that anode biasing can provide a significant improvement in GaAs photocathode lifetime [18].

In retrospect, our conclusion that a biased anode will have an inconsequential effect on the charge lifetime away from the EC was hasty. While the reported observations do support this, most likely during that exploratory study other conditions were dominant, which is supported by the fact that the lifetime at the location away from the EC was lower than at the EC for both the biased and unbiased runs. Importantly, even then it was recognized that lacking a dynamical model of ion transport, the interpretation of those results was semiempirical. It is for this reason that we returned to this work, developing software tools and performing parametric studies to thoroughly characterize the effects of anode biasing.

In this paper, we indeed find that biasing an anode with a positive potential can lead to significant improvement in the charge lifetime by about a factor of 2, notably even when the beam emission location is displaced from the EC. During an extensive 2-year study, daily measurements of QE were performed at the location of electron emission, displaced from the EC, to determine the charge lifetime of a high-polarization, strained-superlattice GaAs/GaAsP photocathode, comparing periods of time when the anode was either biased or grounded. Additionally, a 5 mm diameter circular area of the photocathode surface that was activated to have QE was occasionally measured to determine spatial patterns of QE degradation. To better interpret the experimental results, a computer model of ion production and

tracking leading to photocathode bombardment was created. The simulations were performed with the simulation package General Particle Tracer (GPT) using a newly developed custom element IONATOR [22], which was used to reproduce electron impact ionization of residual gas and to track their motion [23,24].

II. CEBAF LOAD-LOCK PHOTOGUN AND VACUUM CONDITIONS

At CEBAF, spin-polarized electron beams originate from the GaAs/GaAsP photocathode inside a dc high-voltage load-lock photogun using an inverted insulator [25]. The photocathode provides a typical maximum QE of ~1% and spin polarization of ~90% [26]. The photocathode is located within a cathode electrode and is biased at −130 kV using a cable connected to a high-voltage power supply. Two different photoguns were used at CEBAF during this study: initially, a photogun with the cathode shown in Fig. 2(a) was used. It includes an electrostatic shield surrounding the triple-point junction where the cathode and insulator meet vacuum to reduce the field gradient and mitigate the probability of high-voltage breakdown [27,28]. Later, a second cathode electrode shown in Fig. 2(b) was used, which is similar except that the cathode did not include the electrostatic shield. The front surface of both cathodes has a 25° Pierce geometry [29], which focuses the beam through the anode aperture 6 cm downstream of the photocathode.

Fundamental to the design of both photoguns is the intention to achieve the best possible vacuum inside the high-voltage chamber, which serves to minimize IBB and preserve the photocathode QE. The compact design serves to limit the surface area of the high-voltage chamber, with most components degassed prior to construction to minimize the hydrogen outgassing rate [30]. Additionally, the load-locked design isolates the high-voltage chamber using an all-metal gate valve from the photocathode preparation chamber where Cs and NF_3 are routinely used to produce the required negative electron affinity condition of the photocathode.

Two vacuum measurements were performed to estimate the ion production rate: the photogun total pressure was measured using an ionization gauge within the photogun chamber [31], and the relative gas-species composition was measured using a Standard Research Systems residual gas analyzer (RGA200) within the photocathode preparation chamber. The RGA is used when the all-metal gate valve between the chambers is temporarily opened. When the gauges are energized, the ionization gauge is allowed to stabilize for 1 week and the residual gas analyzer for about 1 day.

The total pressure in the photogun, as measured by the ionization gauge, is approximately 2.0×10^{-12} Torr. This value is the nitrogen-equivalent pressure indicated by the ionization gauge divided by 0.46, to account for the higher ionization cross section for hydrogen, which is the dominant gas species within the photogun. In addition, the x-ray background of the ionization gauge, determined to be 1.5×10^{-12} Torr, was first subtracted from the gauge reading [31].

The gas composition in the photogun chamber is typical for a baked system pumped by both ion and nonevaporable
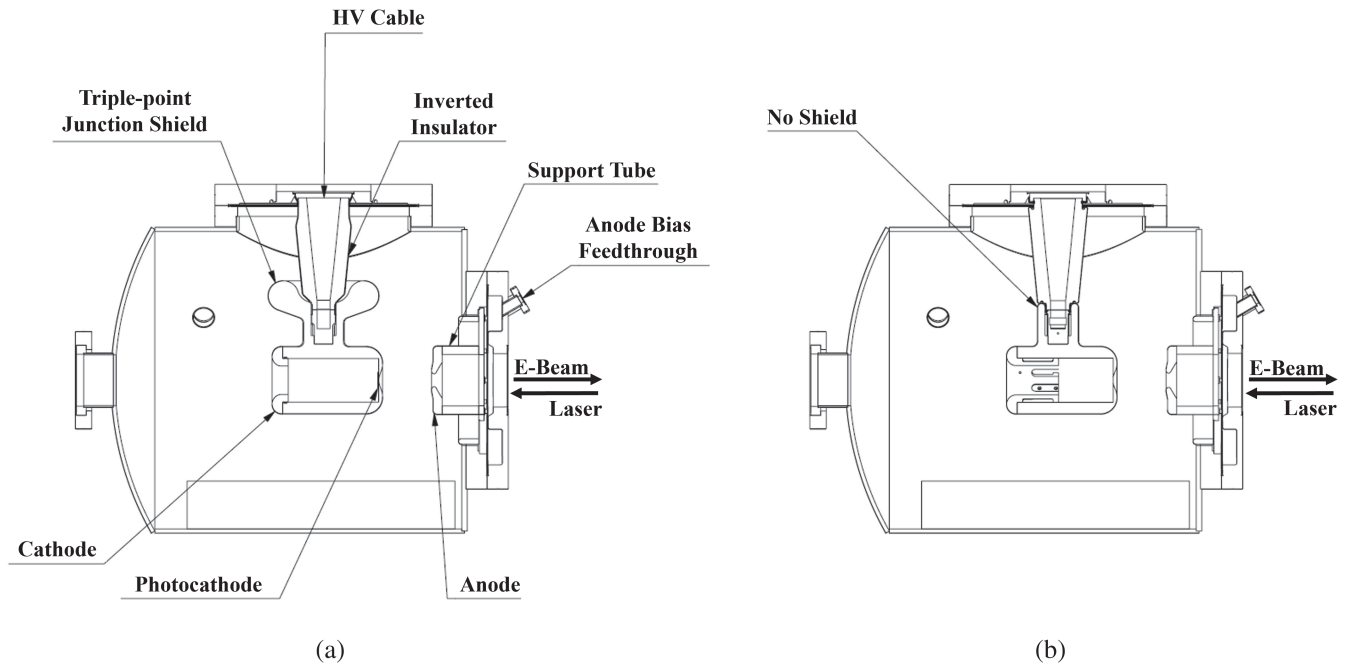

FIG. 2. Schematics of the high-voltage chamber of the CEBAF spin-polarized photogun with (a) and without (b) the tee-shaped electrostatic shield.
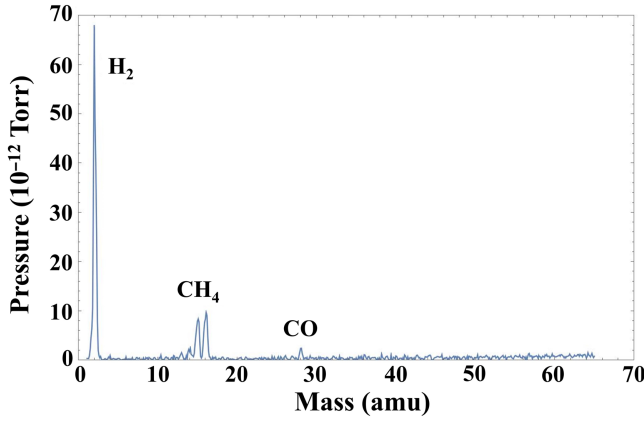
FIG. 3. RGA trace of the photocathode preparation chamber opened to the photogun high-voltage chamber via a 4.5 in. all-metal gate valve.

getter pumps. Figure 3 shows an RGA trace dominated by H_2 with CO and CH_4 in smaller amounts. Applying correction factors of 0.46 for H_2, 1.05 for CO, and 1.40 for CH_4 to account for their respective ionization cross sections

relative to nitrogen [32], the relative abundances of each gas species are: 85% H_2, 10% CH_4, 2% CO, with other gases contributing no more than 3%. Their partial pressures were calculated using the formula:

$$P_{\text{species}} = \frac{(\text{relative abundance})P_{\text{Total}}}{\text{correction factor}}, \qquad (3)$$

where P_{Total} is the total pressure. Using this method, the partial pressures of the three dominant neutral gas species in the photogun were determined to be 1.7×10^{-12} Torr H_2, 2.0×10^{-13} Torr CH_4, and 4.0×10^{-14} Torr CO.

III. CEBAF INJECTOR BEAMLINE AND DRIVE LASER

A schematic of the CEBAF injector beamline extending from the load-lock photogun to the first Faraday cup is shown in Fig. 4. Following the photogun chamber, three pairs of horizontal/vertical steering coils are used to correct for deflections due to the focusing of the cathode/anode
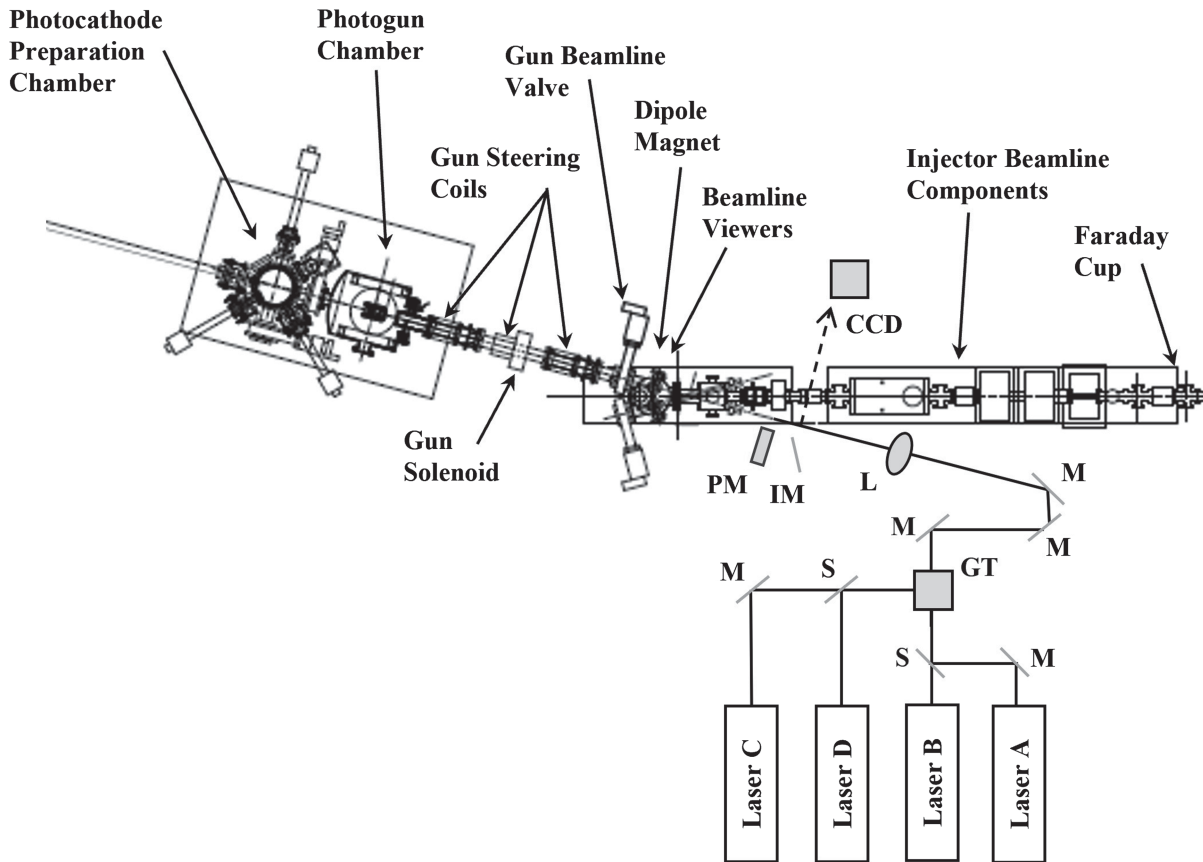

FIG. 4. Schematic of the CEBAF photogun and downstream beamline, highlighting the primary electron beam components used in these measurements and described in the text. Also included is a diagram of the drive laser components used, notably the four rf-synchronized 780 nm polarized lasers (ABCD), mirrors (M), 10/90 combining splitters (S), and a Glan-Thompson polarization cube (GT), which combines the AB and CD paths by polarization. A single steering lens (L) is used to focus the lasers to the same location on the photocathode. A power meter (PM) or insertable mirror (IM) are, respectively, inserted temporarily, to measure the power or spot profile at a CCD camera (CCD).

TABLE I. x and y diameters for each laser using the D4-sigma method.

Laser	A	B	C	D
x diameter (mm)	2.14	2.23	2.05	2.84
y diameter (mm)	1.97	2.15	2.02	2.38

electrodes, the asymmetric inverted insulator geometry, as well as the Earth's magnetic field. The beam is also steered through the solenoid center before passing through a dipole magnet, which bends the beam 15°, allowing for photocathode illumination with laser light at normal incidence. Insertable viewers upstream and downstream of the dipole are used to ensure that the beam is well centered. Beam position monitors, with a resolution of ∼0.1 mm, are used to record the beam orbit upstream and downstream of the dipole.

Four similar lasers [33] (named A, B, C, and D for their respective halls) emit 776.7 ± 1 nm light pulses, as measured with an optical wavelength meter, at repetition rates of 249.5 or 499 MHz, which are synchronized subharmonic frequencies of the CEBAF accelerating frequency of 1497 MHz. The four laser beams are combined with interleaved pulse trains and illuminate the same location on the photocathode [34]. The intensity profile of each laser was measured using a CCD camera at the distance to the photocathode and then fit using BeamGage [35] software to determine its transverse size where photoemission occurs. The sizes were calculated using the D4-sigma method [36], which defines the x and y diameters as four times the standard deviation of the intensity profile, are summarized in Table I. The uncertainties of the beam sizes are estimated by repeated measurements to be ±2%.

IV. QE MEASUREMENT AND ANODE BIASING

The photocathode QE was determined daily using each of the four lasers by recording the laser power required to produce a 10 μA electron beam delivered to a nearby Faraday cup. The QE was then calculated using the formula:

$$\mathrm{QE} = \frac{hc}{e}\frac{I}{\lambda P} \equiv \frac{124 I(\mu A)}{\lambda(\mathrm{nm}) P(\mathrm{mW})}, \qquad (4)$$

where h is Planck's constant, c is the speed of light, e is the elementary charge, P is the laser power, λ is the laser wavelength, and I is the measured current. The total charge produced by the photogun between the daily measurements is also computed by integrating calibrated beam current signals between measurements. The photocathode charge lifetime was then determined using Eq. (1) by fitting the QE measurements over an extended period of time versus the corresponding extracted charge.

Periodically, a "QE scan" was performed, typically at the start or end of a run period weeks apart. During a QE scan,

one laser is scanned using the steering lens in a grid pattern over the photocathode surface covering the active area. At each grid point, a small amount of current is collected by the anode electrode, which is biased positively with a few hundred volts, and the QE is calculated according to Eq. (4). The grid measurements are interpolated to create a contour plot representative of a uniform QE profile across the photocathode surface. Successive contour plots were compared to visualize which areas of the photocathode degraded during each run period.
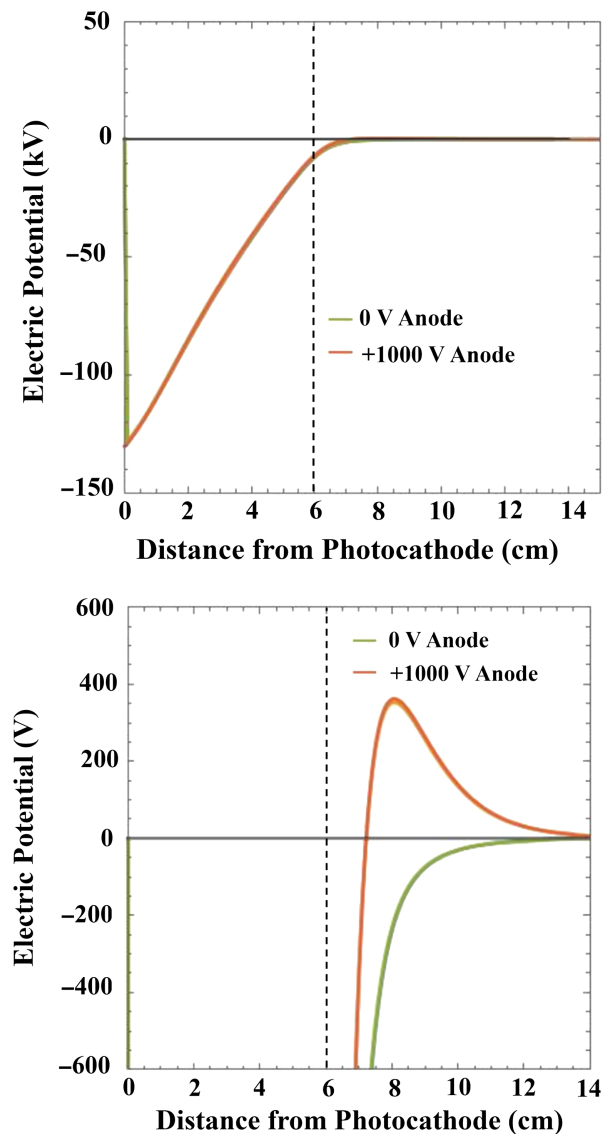

FIG. 5.   The electric potential along the central axis of the beamline for 0 and +1000 V anode configurations of the cathode (the plots are similar for the cathode with and without the electrostatic shield). The top plot shows the full range of the photogun potential, while the bottom plot is an exploded view $|V| \le 600$ V to better see the positive potential peak when the anode is biased. The dashed vertical line denotes the position of the anode ring.

To compare the effect of the anode potential on QE degradation, the anode had to be electrically isolated from the grounded high-voltage chamber. This was accomplished by adding a thin ceramic spacer between the anode and its support tube attached to the grounded downstream flange of the high-voltage chamber (see Fig. 2). The flange was modified to include a high-voltage bakeable vacuum feedthrough in order to control the anode potential using a 5 kV high-voltage power supply.

The electrostatic potential along the central axis of the cathode-anode gap is shown in Fig. 5 when the anode potential is either 0 or +1000 V. Notably, a +1000 V anode bias voltage creates a maximum potential of approximately +350 V on the beamline axis 2 cm downstream of the anode. This value is predicted to be sufficient to repel gas ions from entering the photogun [37]. Consequently, the effect of the anode voltage on QE degradation was measured by periodically changing the output of the power supply between 0 and +1000 V.

V. CHARGE LIFETIME RESULTS

A 2-year study spanning 2019–2020 was performed over three distinct CEBAF run periods. The anode was both grounded and biased during the first two run periods, but due to the success of the technique to improve CEBAF photogun performance, the anode remained biased throughout the third run period.

All of the daily QE measurements made during the 2-year study are plotted in Fig. 6 versus the accumulative charge produced by the CEBAF photogun up to that measurement. The run periods are partitioned with vertical bars, which indicate when the anode potential was changed or the lasers were moved to a different position on the photocathode. When a QE measurement was unphysical, e.g., if there was a readback error of the ammeter or laser power meter then the measurement was discarded.

The dashed lines represent exponential fits of the QE measurement data using Eq. (1) to determine the charge lifetimes. To better visualize QE degradation, only the values for laser A are summarized in Table II, as results of all four lasers are similar. The uncertainty in charge lifetime is dominated by the accumulated charge in a run period. That is, a charge lifetime much larger than the accumulated charge is bound to have a large relative uncertainty.

The beam current was 2 to 3 times higher during run periods 2 and 3 compared to run period 1. The majority of the beam current in each run period was produced using lasers A and C, compared to <10 μA produced using lasers B and D. While higher beam currents have been correlated with lower charge lifetimes [10,21], the effect of the anode bias dominates the effect of the beam current on the charge lifetime.

Importantly, the photocathode charge lifetime changed when the anode bias changed in all but one case (1d). In this case, we speculate the anode bias supply was inadvertently
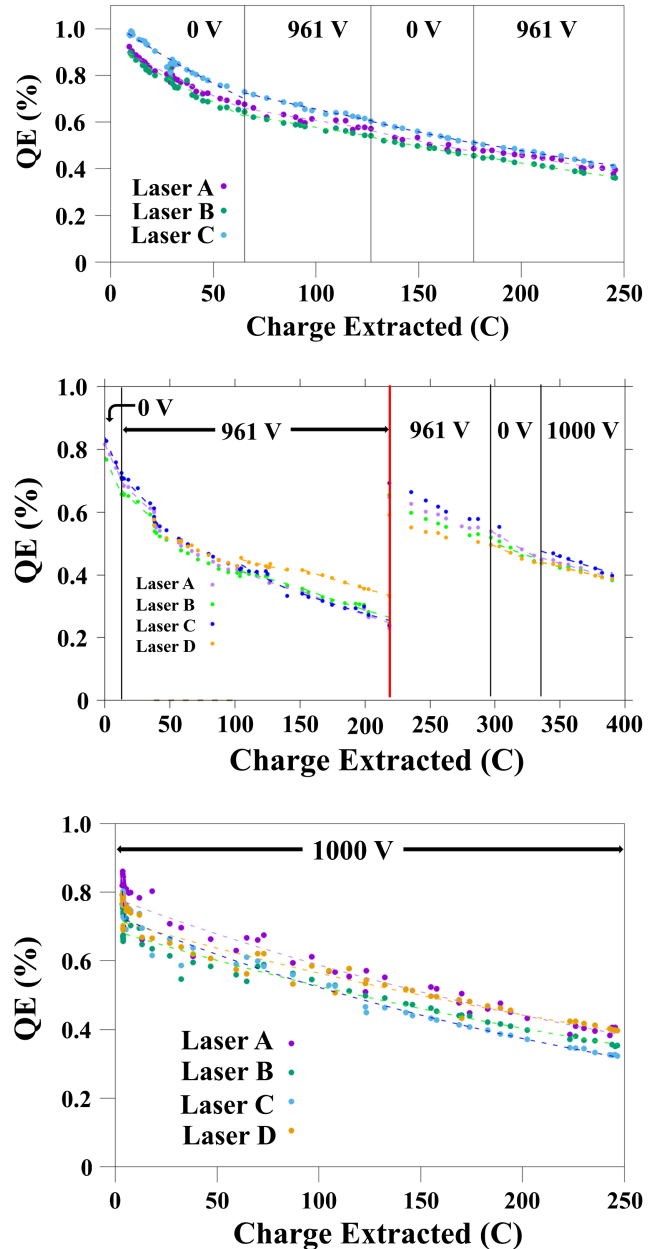

FIG. 6. QE measurements for each laser as a function of charge extracted from the photocathode for run periods 1 (top), 2 (center), and 3 (bottom). The dashed lines are exponential fits [using Eq. (1)] for each set of QE measurements to calculate charge lifetimes. The vertical black lines denote when the anode bias configuration switched. The vertical red line in the center plot denotes when the laser position on the photocathode was moved to an area with higher QE.

powered off (grounded). When considering the remaining cases, the charge lifetime improved by a factor of about 1.8–2.3 when the anode was biased. For the biased configurations, charge lifetimes ranged from 196 to 424 C with an average value of 341 C, whereas for grounded configuration, the charge lifetimes ranged from 86 to 288 C with an average value of 191 C.

TABLE II. Charge lifetime values for laser A for each run period. Uncertainty values correspond to fit errors. The laser spot coordinates are relative to the center of the photocathode.

Run period	Duration (days)	Laser spot (mm)	Beam current (μA)	Total charge extracted (C)	Anode bias (V)	Charge lifetime (C)
1a	40	(−1.00, −1.00)	50–100	65.117	0	181 ± 8
1b	14	(−1.00, −1.00)		61.514	961	424 ± 53
1c	12	(−1.00, −1.00)		50.169	0	288 ± 39
1d	20	(−1.00, −1.00)		68.200	961	303 ± 18
2a	7	(−0.78, 0.00)	150–225	13.026	0	85.8 ± 0.1
2b	57	(−0.78, 0.00)		205.473	961	196 ± 19
2c	10	(1.63, 0.57)		78.516	961	401 ± 10
2d	4	(1.63, 0.57)		33.233	0	208 ± 4
2e	8	(1.63, 0.57)		54.545	1000	370 ± 29
3a	66	(0.88, 0.59)	150–225	246.547	1000	350 ± 14

Subtle operational effects may be observed by carefully inspecting Fig. 6. For example, in run period 2, the QE and lifetimes of all four lasers shifted similarly at ~25 C when the steering lens that positions the lasers was moved. Then later at ~100 C, only the QE and lifetime of the D laser changed when it was inadvertently realigned relative to the others. These differences support the fact that charge lifetime varies spatially over the photocathode surface. However, the biased anode lifetimes remained generally higher than the grounded anode lifetimes independent of laser position.

QE scans were taken at the beginning and end of each run period and when the laser position shifted during run period 2. Plots of the difference between successive QE scan measurements in each run period are shown in Fig. 7. The difference plots show QE degradation primarily occurs near the region of photoemission, yet significant degradation occurs elsewhere across the photocathode as well.

VI. SIMULATING ION BACK-BOMBARDMENT

To interpret the experimental results, a framework for IBB particle tracking simulations was developed using the simulation tool General Particle Tracer (GPT) [23]. In each simulation, an electron beam distribution begins at the photocathode, accelerates through the electrostatic model of the photogun, and finally transports through magnetic field maps of the beamline elements. Because the dipole (located 1.67 m downstream of the photocathode) is tuned for a 130 keV electron beam, an ion produced downstream of the dipole cannot pass through the dipole and reach the photocathode. For this reason, the electron distribution is tracked to the first viewer, located 1.54 m downstream of the photocathode.

Electron impact ionization is not a built-in feature of GPT. The C++ custom element IONATOR was developed and implemented to simulate the ion production of H_2, CO, or CH_4 molecules along the trajectory of the beam distribution [24]. The relative concentrations of each gas species, described in Sec. II, are included to allow for accurate ion production rates. The velocity distribution of each residual gas is assumed to follow a Maxwellian distribution at room temperature. IONATOR uses Monte Carlo algorithms to determine the ion production rate and the secondary electron kinetic energy based on user-defined gas pressures, the ionization cross section, and the secondary electron differential cross section. The energy and momentum of the resulting secondary electron, scattered electron, and ion are calculated using relativistic kinematics, taking into account the respective conservation laws. Particles are then tracked until they reach the photocathode or a simulation boundary. The formalism and examples of the ionization
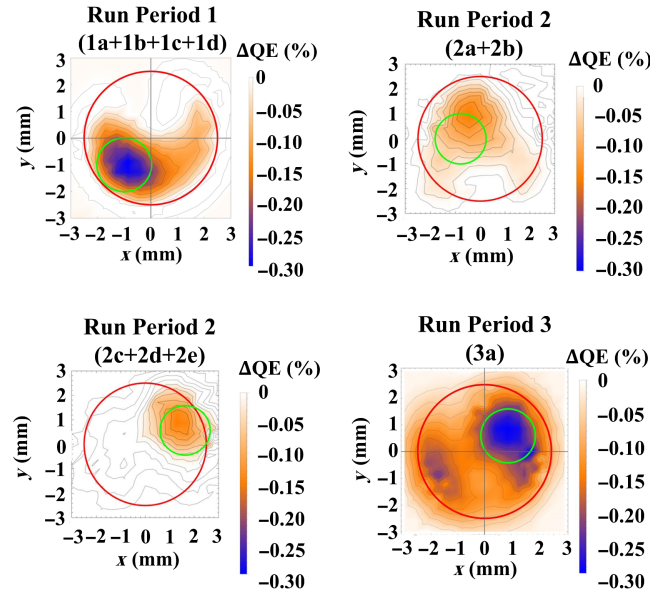

FIG. 7. QE difference scans showing spatial degradation of the photocathode during the specified run period sections, which correspond to the run period sections in Table II. Separate difference scans are shown for each laser position used in run period 2. The red circle denotes the 5 mm diameter active area and the green circle denotes the 2 mm diameter laser spot.

cross section, ion production rate, the secondary electron differential cross section, and Maxwellian distribution for each residual gas species considered in this work are shown in the Appendix.

Earlier versions of IONATOR derived the energy of the ion immediately following ionization from a Maxwellian distribution with the most probable energy fixed at 4 eV [38,39]. Theoretical formulas or empirical data predicting the fraction of the electron energy imparted to the ion are currently lacking. Until measurement or theory improves, IONATOR instead allows the user to specify the fraction k of the total energy E_{final} that the ion will receive:

$$E_{ion} = kE_{final} = k(E_{prim} + E_{gas} - E_{sec} - B), \quad (5)$$

where E_{prim}, E_{gas}, and E_{sec} are the kinetic energies of the primary electron, target gas particle, and secondary electron, respectively, B is the ionization energy, and k is a real number between 0 and 1. As will be described in Sec. VIII, the k value chosen in the simulations is an important parameter for IBB.

Separate simulations were made for each anode bias configuration used in each run period. The electron distribution is generated at the photocathode location with an initial kinetic energy equal to the mean transverse energy of 0.13 eV [40]. The distribution accelerates to 130 keV using a 3D electrostatic model of the CEBAF photogun created using CST software [41], using independent models of the photogun for grounded and biased anode configurations and for the two cathode electrode shapes in Fig. 2. The simulations also include field maps of the three steering coils and solenoid. Figure 8 shows a diagram of the photogun, the initial beamline, and the locations and dimensions of the field maps. The simulation is bounded by the photocathode, viewer, and inner surface of the beam pipe, which is 0.06 m in diameter. Any simulation particle that reaches the boundary is removed from the simulation. The coordinate system is such that the origin is at the center of the photocathode, the z axis is normal to the
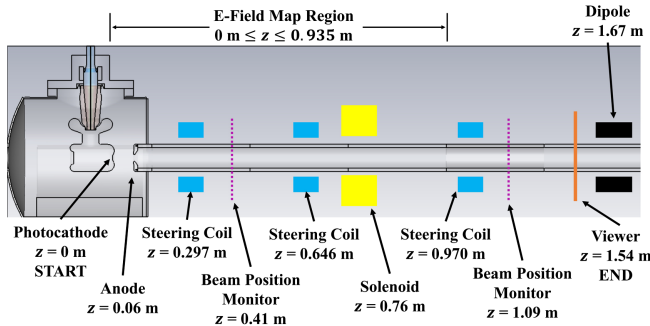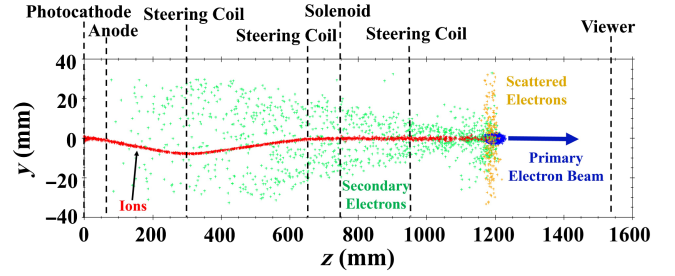

FIG. 9.   Example of a GPT/IONATOR run depicting a side view of the primary electron beam (blue) traveling through the CEBAF injector beamline and creating ions (red). In doing so, secondary electrons (green) are created and the primary electron scatters away (orange) from the beam. The snapshot corresponds to 7 ns after the electron bunch leaves the photocathode.

photocathode and points along the beamline axis, the y axis points vertically upward, and the x axis points to the left when looking downstream.

Figure 9 shows a snapshot of a simulation corresponding to 7 ns after the electron bunch leaves the photocathode in run period 1. Here, the electrons receive an expected downward deflection due to the electrostatic shield [42] used in run period 1, and steering coils recenter the beam along the beamline axis.

VII. SIMULATION RESULTS

Simulation results for the predicted IBB for run period 1 are shown in Fig. 10, where $k = 10^{-7}$ was chosen, as discussed in Sec. VIII below. The results are color-coded by
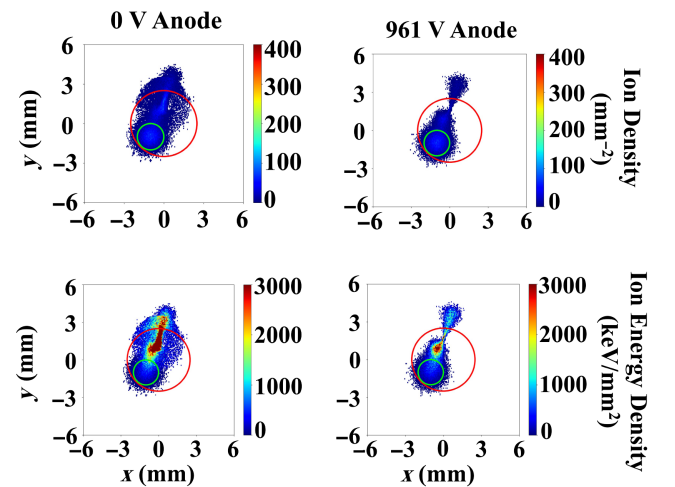

FIG. 10.   Density (top) and energy density (bottom) distributions of simulated back-bombarding ions at the photocathode for 0 V (left) and 961 V (right) anode configurations using the cathode with the electrostatic shield [Fig. 2(a)] used in run period 1, assuming $k = 10^{-7}$. The red circle denotes the 5 mm diameter active area and the green circle denotes the 2 mm diameter laser spot.

FIG. 8.   Diagram showing the locations of the electric and magnetic field maps used in the GPT simulations (not to scale).

ion density and ion energy density at the photocathode for both the biased and grounded configurations. While IBB covers the QE areas in all cases, the ion and energy-weighted distributions are both significant at the laser spot, consistent with where most QE degradation occurred during run period 1 (see Fig. 7). Comparing the plots for the 0 V anode vs the 961 V anode, fewer ions reach the photocathode when the anode is biased, resulting in less ion density and ion energy density within the laser spot.

It is also notable that the ion energy-weighted simulations show significant IBB along a "trench" from the laser spot center to approximately 4.5 mm away from the laser spot. This second location is approximately 1.5 mm above the nominal cathode electrode center. This effect has been experimentally observed [9,12,20] and may now be attributed to IBB experiencing a transverse kick in the direction of the EC.

For comparison, these simulations were repeated using the photogun without the electrostatic shield. The corresponding ion density and ion energy density plots are shown in Fig. 11. Again, fewer ions reach the photocathode when the anode is biased. Comparing Fig. 10 to Fig. 11, it is clear the IBB distributions depend on whether the cathode includes the electrostatic shield, which alters the transverse electric field in the cathode-anode gap [27]. While the electrostatic shield used in run period 1 produces a large and unwanted electron beam deflection, it also serves to reduce the number of back-bombarding ions reaching the active area, as these ions experience a stronger vertical kick with the shield than without.

VIII. DISCUSSION

The experimental results show a clear benefit of biasing the anode to improve charge lifetime. In all three run periods, the charge lifetime with the biased anode configuration was higher than the charge lifetime of the preceding grounded anode configuration. In fact, the charge lifetime for run period 3, when the anode configuration remained biased, is higher than all grounded anode charge lifetimes in run periods 1 and 2. The charge lifetimes for grounded and biased anode configurations for run periods 1 and 2 are compared in Table III by taking the ratio of the biased anode charge lifetime to grounded anode charge lifetime. Because the anode remained biased throughout run period 3 and different run conditions were used (e.g., different laser spot position), no improvement ratios were calculated using the charge lifetime during run period 3. Taking the ratio of the average biased and grounded anode charge lifetimes, the average charge lifetime improvement is 1.80 ± 0.54.

While the improvement ratios in Table III remain above unity in run periods 1 and 2, it is interesting that the ratios decrease throughout each run period. The decrease may be explained in part by the Gaussian transverse distribution of back-bombarding ions on the lasers spot due to the Gaussian transverse distribution of the electron beam creating the ions. As a result, a higher intensity of back-bombarding ions reaches the photocathode within the center of the laser spot compared to the edges of the laser spot, implying that most of the QE degradation, and thus charge lifetime improvement with the biased anode, occurs in the beginning of the run period.

The QE difference scans in Fig. 7 show that, while nearly all of the active area experiences QE degradation to some degree, the majority of the QE degradation occurs at or near the laser spot. While the relative positions of the four lasers, which overlap at the laser spot position, have been shown to be stable over many months, the overall laser spot position on the photocathode may drift due to thermal variations between the laser table and the photogun table over long periods of time, which may explain the offset of the highest QE degradation seen during the first two run period sections of run period 2. The highest QE degradation during run period 1 is at the laser spot, which is consistent
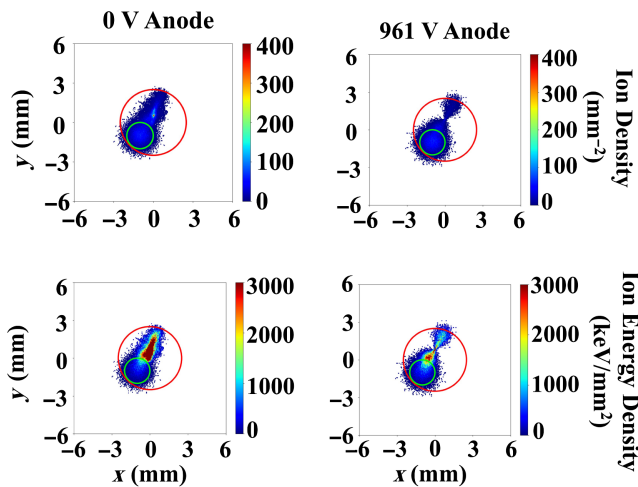

FIG. 11. Density (top) and energy density (bottom) distributions of simulated back-bombarding ions at the photocathode for 0 V (left) and 961 V (right) anode configurations using the cathode with no electrostatic shield [Fig. 2(b)], assuming $k = 10^{-7}$. The red circle denotes the 5 mm diameter active area and the green circle denotes the 2 mm diameter laser spot. The laser position is the same as the laser position used in run period 1 for comparison with Fig. 10.

TABLE III. Charge lifetime improvement ratios for laser A during run periods 1 and 2. $\tau_1, \tau_2, \tau_3, \dots$ correspond to the first, second, third,... charge lifetimes in each run period.

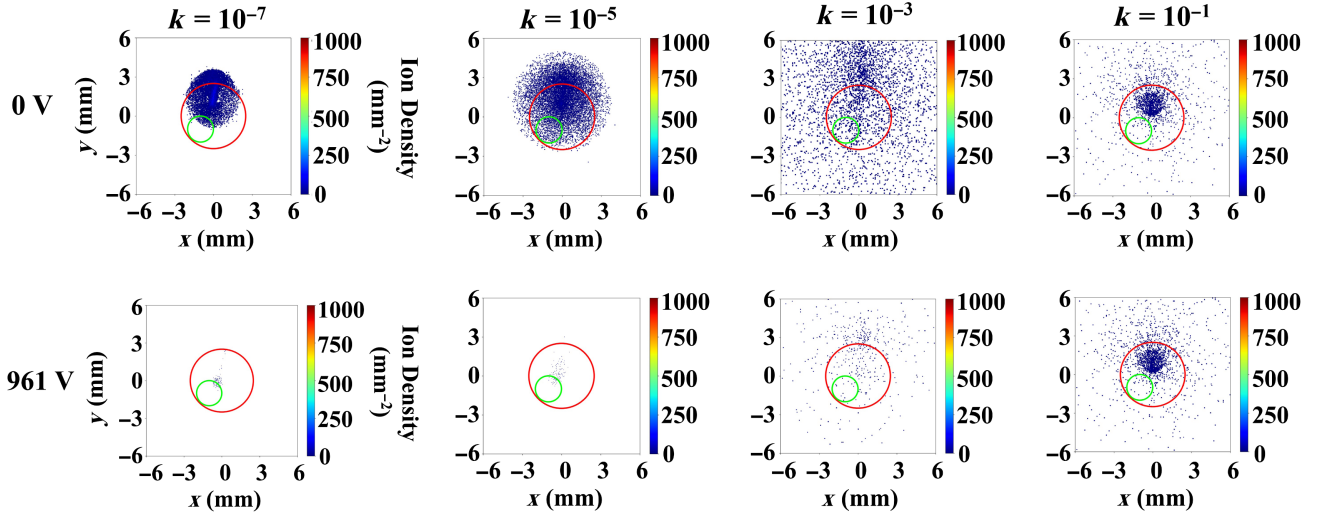| Run period	Improvement ratio	Value
1	τ_2/τ_1	2.34 ± 0.31
	τ_4/τ_3	1.05 ± 0.16
2	τ_2/τ_1	2.28 ± 0.22
	τ_3/τ_4	1.93 ± 0.06
	τ_5/τ_4	1.78 ± 0.14

FIG. 12. Plots comparing the density of back-bombarding ions originating downstream of the anode for grounded anode simulations (top row) and biased anode simulations (bottom row) for run period 1 (using the cathode with the electrostatic shield), with the ion energy fraction $k = 10^{-7}$ (left), $k = 10^{-5}$ (center left), $k = 10^{-3}$ (center right), and $k = 10^{-1}$ (right). The red circle denotes the 5 mm diameter active area and the green circle denotes the 2 mm diameter laser spot.

with the area of highest ion density in grounded and biased anode simulations in Fig. 10. However, because the QE was not originally uniform throughout the active area at the beginning of run period 1, with zero QE within the vicinity of the EC, it is unclear whether ion density or energy density contributes more to QE reduction.

While the QE reduction near the laser spot in run period 3 ($x = 1$ mm, $y = 1$ mm) was predicted by simulation, it is worth noting that the observed broader reduction in QE was not expected. This type of broader reduction is consistent with increased vacuum load, or possibly even small levels of field emission, which could have occurred during the 66 days between the QE scans. In prior run periods spanning more than a year, this was not observed, which does suggest there was some additional process of QE reduction different than the beam-based IBB being studied.

To demonstrate the effect that the ion energy fraction k has on the simulated IBB distributions, Fig. 12 compares the density distribution of IBB originating downstream of the anode for grounded and biased anode configurations with the electrostatic shield and with k ranging from 10^{-1} to 10^{-7}. The value of k has a clear impact on whether the ion reaches the photocathode. If the kinetic energy of an ion downstream of the anode is lower than the peak anode potential, then the biased anode potential will repel it away from the photocathode. If its kinetic energy exceeds the biased anode potential, then the ion can pass through the anode aperture and reach the photocathode. As a result, the difference in ion distribution between grounded and biased anode simulations becomes greater for smaller values of k. In addition, back-bombarding ions originating downstream of the peak anode potential experience more deflection toward the EC for smaller values of k before reaching the photocathode due to their lower energies.

To quantify the reduction of back-bombarding ions when biasing the anode, Table IV shows ratios of back-bombarding ions incident on the laser spot between grounded and biased anode configurations for run period 1 with k between 10^{-1} and 10^{-7}. The ratios are either weighted or unweighted by the kinetic energy of the ions and are calculated using the formulas:

$$\text{Unweighted ratio} = \frac{\sum N_{0\ \text{V}}/Q_{0\ \text{V}}}{\sum N_{961\ \text{V}}/Q_{961\ \text{V}}}, \qquad (6)$$

$$\text{Energy-weighted ratio} = \frac{\sum E_{0\ \text{V}}/Q_{0\ \text{V}}}{\sum E_{961\ \text{V}}/Q_{961\ \text{V}}}, \qquad (7)$$

where N is the number of ions, E is the kinetic energy of the back-bombarding ion upon impact, and Q is the total electron charge extracted from the photocathode from all run period sections. The unweighted ratios indicate at most a 9.2% difference in the number of ions incident on the

TABLE IV. Ion ratios between grounded and biased anode simulations for back-bombarding ions incident on the laser spot for run period 1.

k	Unweighted ion ratio	Energy-weighted ion ratio
10^{-7}	1.092	1.808
10^{-6}	1.073	1.577
10^{-5}	1.077	1.512
10^{-4}	1.030	1.164
10^{-3}	1.004	1.038
10^{-2}	1.044	1.065
10^{-1}	1.056	1.258

laser spot between grounded and biased anode simulations when $k = 10^{-7}$. However, the energy-weighted ion ratio at this value of k is 1.808, which is consistent with the average charge lifetime improvement, indicating that the energy of the back-bombarding ion plays a significant role in QE reduction. The energy-weighted ion ratios for $k = 10^{-6}$ and 10^{-5} are also consistent with the average charge lifetime improvement due to its large uncertainty.

Next, we explored if an elevated beamline vacuum downstream of the anode could explain the charge lifetime improvement of 1.80 between grounded and biased anode conditions. To do this, a simulation study was performed where, for different values of k between 10^{-7} and 10^{-1}, the beamline pressure was allowed to increase up to 10 times the total photogun pressure (i.e., up to 2.0×10^{-11} Torr), as a MOLFLOW+ simulation predicts that the beamline pressure is unlikely to be more than this [43,44]. The unweighted and energy-weighted ratios were then calculated for each k using Eqs. (6) and (7). Finally, the required pressure to produce an ion ratio of 1.80 was found. A plot of the required beamline pressures vs k for both the unweighted and energy-weighted ratios is shown in Fig. 13. Considering the energy-weighted ion ratio data, reasonable values for k are 10^{-1} and between 10^{-7} and 10^{-4}.

In summary, a biased anode nearly doubles the charge lifetime of the photocathode and can be used in experiments that use GaAs photocathodes to create polarized electron beams and require high charge lifetimes. Further, the use of an ion generating and beam tracking simulation model, such as the custom element IONATOR developed for this project, was instrumental in better explaining and exploring IBB, which remains the limiting factor in the charge lifetime of GaAs-based photocathodes in modern, ultrahigh vacuum, dc high-voltage photoguns.

APPENDIX: IONIZATION EQUATIONS USED IN IONATOR

IONATOR uses the form of the cross section formula for electron impact ionization in [45], originally derived by Bethe [38]:

$$\sigma(\mathrm{m}^2) = \frac{1.872 \times 10^{-24} A_1}{\beta_e^2} f(T)$$
$$\times \left[\ln\left(7.515 \times 10^4 A_2 \beta_e^2 \gamma^2\right) - \beta_e^2\right],$$
$$f(T) = 1 - \frac{B}{T}, \tag{A1}$$

where β_e and γ are the primary electron relativistic factors, A_1 and A_2 are the empirical constants that depend on the gas species [46], and the function $f(T)$ is used to fit σ at low energies when $T \approx B$. Figure 14 shows a log-log plot of the ionization cross section as a function of primary electron kinetic energy for H_2, CO, and CH_4.

The ion production rate per unit length is given by

$$\frac{dN_{\mathrm{ion}}}{dt}\left(\frac{1}{d}\right) = \rho\sigma\frac{I}{e}, \tag{A2}$$

where ρ is the gas density, I is the electron current, and e is the elementary charge. Figure 15 shows a log-log plot of the ion production rate per unit length as a function of primary electron kinetic energy for H_2, CO, and CH_4. The ionization cross section and ion production rate are highest at low primary electron kinetic energies. For a 100 eV electron beam with a current of 100 μA and ionizing H_2 gas at a pressure of 1.7×10^{-12} Torr, the ionization cross
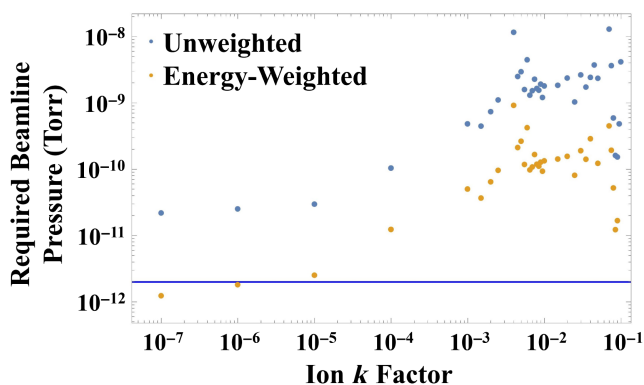

FIG. 13. Plot of vacuum pressure within the beamline downstream of the peak anode potential required to produce an unweighted (blue) or energy-weighted (orange) ion ratio of 1.8 at the laser spot, as a function of k. The horizontal dark blue line represents the total photogun pressure of 2.0×10^{-12} Torr for reference.
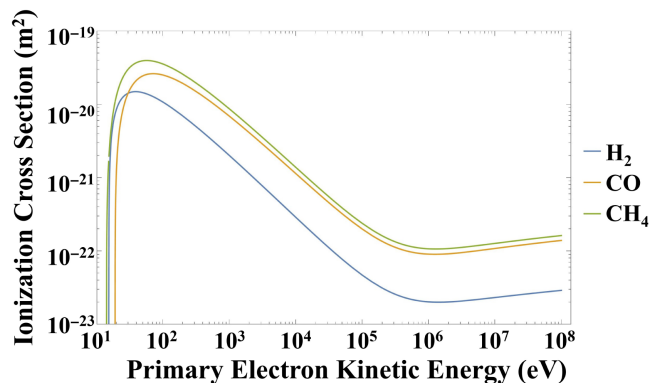

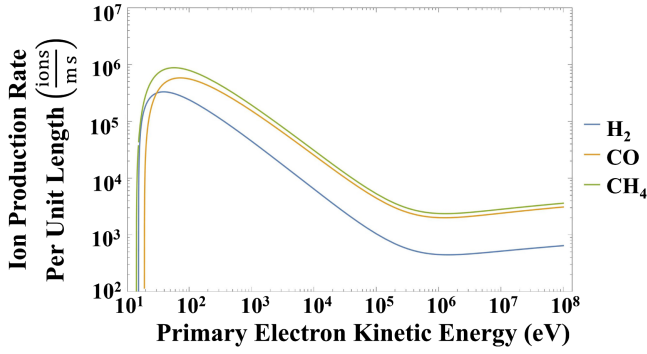FIG. 14. The ionization cross section as a function of primary electron kinetic energy for H_2, CO, and CH_4.

FIG. 15. The ion production rate per unit length as a function of primary electron kinetic energy for H_2, CO, and CH_4.
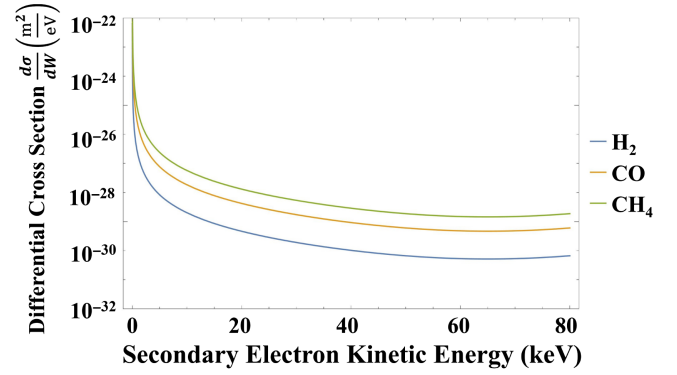

FIG. 16. The secondary electron differential cross section $d\sigma/dW$ for H_2, CO, and CH_4 as a function of secondary electron kinetic energy.

section is 1.1×10^{-20} m^2 and the ion production rate per unit length is 4.1×10^6 $\frac{H_2^+}{ms}$.

The possible postionization kinetic energies W of a secondary electron originating in subshell i as a function of the primary electron energy T are given by the secondary electron differential cross section (SEDCS) derived in the binary encounter dipole model [47]:

$$\frac{d\sigma(W,T)}{dW} = \frac{S}{B(t+u+1)}\left[\frac{(\frac{N_i}{N})-2}{t+1}\left(\frac{1}{w+1}+\frac{1}{t-w}\right)\right.$$
$$+\left(2-\frac{N_i}{N}\right)\left(\frac{1}{(w+1)^2}+\frac{1}{(t-w)^2}\right)$$
$$\left.+\frac{\ln(t)}{N(w+1)}\frac{df(w)}{dw}\right],$$
$$S = 4\pi a_0^2 N R^2/B^2,$$
$$t = T/B,$$
$$u = U/B,$$
$$w = W/B,$$
$$N_i = \int_0^\infty \frac{df}{dw}dw, \qquad (A3)$$

where a_0 is the Bohr radius, R is the Rydberg energy, N is the number of electrons in the subshell of the gas molecule prior to ionization, U is the average kinetic energy of electrons in the subshell, and df/dw is the differential oscillator strength. Because the differential oscillator strengths for CO and CH_4 are not well known, Kim and Rudd gave an approximation for the differential cross section [47]:

$$\frac{d\sigma(W,T)}{dw} = \frac{S}{t+u+1}\left[\frac{1}{(t-w)^2}+\frac{1}{(w+1)^2}\right.$$
$$-\frac{1}{t+1}\left(\frac{1}{t-w}+\frac{1}{w+1}\right)$$
$$\left.+\ln(t)\left(\frac{1}{(t-w)^3}+\frac{1}{(w+1)^3}\right)\right]. \qquad (A4)$$

Plots of the SEDCS for H_2, CO, and CH_4 as a function of secondary electron kinetic energy are shown in Fig. 16. The secondary electron is likely to have a very low kinetic energy relative to the primary electron postionization. Figure 14 suggests that secondary electrons have a higher ionization cross section than the primary electron beam ($T = 130$ keV) and are thus more likely to ionize. However, since there are several orders of magnitude more electrons in the electron beam than secondary electrons generated from ionization, it is much more likely that ions are generated from the electron beam than from secondary electrons.

The residual gas species within the accelerator are assumed to be at room temperature (293.15 K). Assuming the residual gas follows the ideal gas law, the velocity distributions can be modeled using a Maxwellian distribution of the form:

$$F(v)dv = \sqrt{\frac{2}{\pi}}\frac{v^2\exp-\frac{v^2}{2a^2}}{a^3}dv,$$
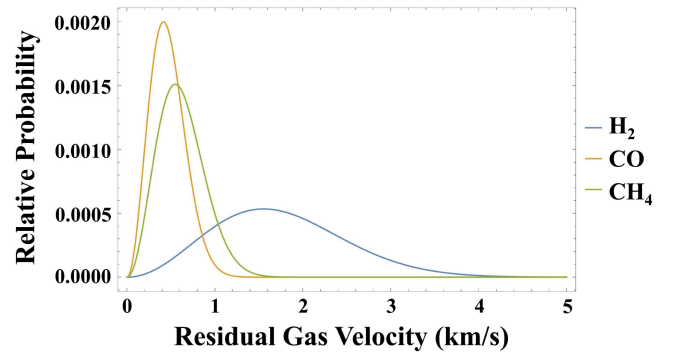$$a = \left(\frac{k_B T}{m}\right)^{\frac{1}{2}}, \qquad (A5)$$

FIG. 17. The velocity distribution of H_2, CO, and CH_4, assuming each residual gas species follows a Maxwellian distribution at room temperature.

TABLE V.   Most probable and average velocities for H_2, CO, and CH_4 at room temperature.

Gas species	v_{prob} (km/s)	v_{avg} (km/s)
H_2	1.56	1.75
CO	0.416	0.469
CH_4	0.550	0.620

where k_B is the Boltzmann constant and $\mathcal{T}$ is the gas temperature.

Figure 17 shows plots of the velocity distributions for H_2, CO, and CH_4 at room temperature. Their average and most probable velocities are given in Table V. The average and most probable kinetic energy of all three gas species are roughly the same: $E_{prob} \approx 25.3$ meV and $E_{avg} \approx 32.3$ meV.

---

[1] M. J. Fero (SLD), in *Proceedings of the 14th International Conference on Physics in Collision, PHYSCOLL-1994, Tallahassee, FL* (1994), pp. 35–49, https://inspirehep.net/literature/379694.

[2] G. Moortgat-Pick *et al.*, Phys. Rep. **460,** 131 (2008).

[3] J. Arrington, K. de Jager, and C. F. Perdrisat, J. Phys. Conf. Ser. **299,** 012002 (2011).

[4] D. Adhikari *et al.* (PREX), Phys. Rev. Lett. **126,** 172502 (2021).

[5] P. A. Adderley *et al.*, Phys. Rev. Accel. Beams **27,** 084802 (2024).

[6] M. L. Stutzman and J. Grames, AIP Conf. Proc. **1149,** 1032 (2009).

[7] V. Shutthanandan, Z. Zhu, M. L. Stutzman, F. E. Hannon, C. Hernandez-Garcia, M. I. Nandasiri, S. V. N. T. Kuchibhatla, S. Thevuthasan, and W. P. Hess, Phys. Rev. ST Accel. Beams **15,** 063501 (2012).

[8] W. Liu, Y. Chen, W. Lu, A. Moy, M. Poelker, M. L. Stutzman, and S. Zhang, Appl. Phys. Lett. **109,** 252104 (2016).

[9] C. Hernandez-Garcia *et al.*, Phys. Rev. Accel. Beams **22,** 113401 (2019).

[10] J. Grames, D. Moser, P. Adderley, J. Hansknecht, R. Kazimi, M. Poelker, M. L. Stutzman, R. Suleiman, and S. Zhang, in *Proceedings of the 2017 International Workshop on Polarized Sources, Targets, and Polarimetry, PSTP-2017, Daejeon, Republic of Korea* (2018), p. 014, https://pos.sissa.it/324/014.

[11] S. Full, A. Bartnik, I. V. Bazarov, J. Dobbins, B. Dunham, and G. H. Hoffstaetter, Phys. Rev. Accel. Beams **19,** 034201 (2016).

[12] O. Rahman, E. Wang, I. Ben-Zvi, J. Biswas, and J. Skaritka, Phys. Rev. Accel. Beams **22,** 083401 (2019).

[13] L. Cultrera, A. Galdi, J. K. Bae, F. Ikponmwen, J. Maxson, and I. Bazarov, Phys. Rev. Accel. Beams **23,** 023401 (2020).

[14] J. K. Bae, L. Cultrera, P. DiGiacomo, and I. Bazarov, Appl. Phys. Lett. **112,** 154101 (2018).

[15] G. A. Mulhollan and J. C. Bierman, J. Vac. Sci. Technol. A **26,** 1195 (2008).

[16] M. Herbert, J. Enders, M. Poelker, and C. Hernandez-Garcia, in *Proceedings of the 18th International Workshop on Polarized Sources, Targets, and Polarimetry, PSTP-2019, Knoxville* (2020), p. 042, https://pos.sissa.it/324/016.

[17] N. Kurichiyanil, J. Enders, Y. Fritzsche, and M. Wagner, J. Instrum. **14,** P08025 (2019).

[18] E. Wang, O. Rahman, J. Skaritka, W. Liu, J. Biswas, C. Degen, P. Inacker, R. Lambiase, and M. Paniccia, Phys. Rev. Accel. Beams **25,** 033401 (2022).

[19] E. Pozdeyev, Phys. Rev. ST Accel. Beams **10,** 083501 (2007).

[20] J. Grames, P. A. Adderley, J. Brittian, J. Clark, J. Hansknecht, D. Machie, M. Poelker, E. Pozdeyev, M. L. Stutzman, and K. Surles-Law, AIP Conf. Proc. **980,** 110 (2008).

[21] J. Grames, R. Suleiman, P. A. Adderley, J. Clark, J. Hansknecht, D. Machie, M. Poelker, and M. L. Stutzman, Phys. Rev. ST Accel. Beams **14,** 043501 (2011).

[22] IONATOR is licensed under the Creative Commons Attribution 4.0 International License. To view a copy of this license, please visit http://creativecommons.org/licenses/by/4.0/ or send a letter to Creative Commons, PO Box 1866, Mountain View, CA 94042, USA.

[23] General Particle Tracer (GPT) version 3.39, http://www.pulsar.nl/gpt (2019).

[24] J. T. Yoskowitz, G. A. Krafft, G. Palacios-Serrano, S. Wijethunga, J. Grames, J. Hansknecht, C. Hernandez-Garcia, M. Poelker, M. L. Stutzman, R. Suleiman, and S. B. van der Geer, in *Proceedings of the 12th International Particle Accelerator Conference, IPAC-2021, Campinas, Brazil* (JACoW, Geneva, Switzerland, 2021), pp. 2840–2842, 10.18429/JACoW-IPAC2021-WEPAB104.

[25] P. A. Adderley, J. Clark, J. Grames, J. Hansknecht, K. Surles-Law, D. Machie, M. Poelker, M. L. Stutzman, and R. Suleiman, Phys. Rev. ST Accel. Beams **13,** 010101 (2010).

[26] C. K. Sinclair, P. A. Adderley, B. M. Dunham, J. C. Hansknecht, P. Hartmann, M. Poelker, J. S. Price, P. M. Rutt, W. J. Schneider, and M. Steigerwald, Phys. Rev. ST Accel. Beams **10,** 023501 (2007).

[27] G. Palacios-Serrano, Electrostatic design and characterization of a 200 keV photogun and Wien spin rotator, Ph.D. thesis, Old Dominion University, Norfolk, VA, 2021, 10.25777/mf9f-r453.

[28] Y. Wang, Development of a 300 KV DC high voltage photogun and beam based studies of alkali antimonide photocathodes, Ph.D. thesis, Old Dominion University, Norfolk, VA, 2018, 10.25777/smqt-t242.

[29] J. R. Pierce, J. Appl. Phys. **11,** 548 (1940).

[30] M. A. Mamun, A. A. Elmustafa, M. L. Stutzman, P. A. Adderley, and M. Poelker, J. Vac. Sci. Technol. A **32,** 021604 (2013).

[31] Leybold, Leybold extractor gauge, model IE 514 with IONIVAC IM 520 controller, https://www.leyboldproducts.com/products/measuring-and-analysis-instruments/pressure-measurement/ultra-high-vacuum-gauges/ (2022).

[32] MKS, Gas correction factors for ionization vacuum gauges, https://www.mks.com/n/gas-correction-factors-for-ionization-vacuum-gauges (2022).

[33] J. Hansknecht and M. Poelker, Phys. Rev. ST Accel. Beams **9,** 063501 (2006).

[34] P. A. Adderley, D. Bullard, Y. C. Chao, C. H. Garcia, J. Grames, J. Hansknecht, A. Hofler, R. Kazimi, J. Musson, C. Palatchi, K. Paschke, M. Poelker, G. Smith,

M. L. Stutzman, R. Suleiman, and Y. Wang, Nucl. Instrum. Methods Phys. Res., Sect. A **1046**, 167710 (2023).

[35] BeamGage v. 6.15.3, https://www.ophiropt.com/ (2022).

[36] ISO 11146:2021, Test methods for laser beam widths, divergence angles and beam propagation ratios, Standard (International Organization for Standardization, 2021), https://www.iso.org/standard/77769.html.

[37] J. T. Yoskowitz, Ion production and mitigation in DC high-voltage photoguns, Ph.D. thesis, Old Dominion University, Norfolk, VA, 2022, 10.25777/wm40-aj78.

[38] H. Bethe, Ann. Phys. (Leipzig) **397**, 325 (1930).

[39] E. W. McDaniel, *Atomic Collisions: Electron and Photon Projectiles* (Wiley, New York, NY, 1989).

[40] W. M. S. Wijethunga, Space charge effects in low energy magnetized electron beams, Ph.D. thesis, Old Dominion University, Norfolk, VA, 2021, 10.25777/pgey-pd89.

[41] CST Studio Suite, http://www.cst.com (2019).

[42] G. Palacios-Serrano, F. E. Hannon, C. Hernandez-Garcia, M. Poelker, and H. Baumgart, Rev. Sci. Instrum. **89**, 104703 (2018).

[43] MOLFLOW+, https://molflow.web.cern.ch/ (2022).

[44] M. L. Stutzman, Jefferson Lab Injector Beamline Upgrade: Phase 1, Report No. JLAB-TN-24-048, 2024, https://jlabdoc.jlab.org/docushare/dsweb/Get/Document-291181/24-048_.pdf.

[45] M. Reiser, *Theory and Design of Charged Particle Beams* (Wiley VCH Verlag GmbH, Weinheim, Germany, 2008), 10.1002/9783527617623.

[46] F. F. Rieke and W. Prepejchal, Phys. Rev. A **6**, 1507 (1972).

[47] Y.-K. Kim and M. E. Rudd, Phys. Rev. A **50**, 3954 (1994).